Applied Surface Science 426 (2017) 1121–1132

Contents lists available at ScienceDirect

Applied Surface Science

journal homepage: www.elsevier.com/locate/apsusc

Full Length Article

High performance polydopamine-functionalized mesoporous silica nanospheres for U(VI) removal

Linfeng Bai[a,b], Shengxia Duan[c], Wanquan Jiang[a,*], Mei Liu[a], Sheng Wang[a], Min Sang[a], Xinglong Gong[b,*], Jiaxing Li[c], Shouhu Xuan[b,*]

[a] Department of Chemistry, Collaborative Innovation Center of Suzhou Nano Science and Technology, University of Science and Technology of China (USTC), Hefei 230026, PR China
[b] CAS Key Laboratory of Mechanical Behavior and Design of Materials, Department of Modern Mechanics, USTC, Hefei 230027, PR China
[c] Key Laboratory of Novel Thin Film Solar Cells, Institute of Plasma Physics, Chinese Academy of Sciences, P.O. Box 1126, Hefei 230031, PR China

ARTICLE INFO

Article history:
Received 10 April 2017
Received in revised form 30 June 2017
Accepted 28 July 2017
Available online 31 July 2017

Keywords:
Dopamine
Mesoporous silica
Adsorption
U(VI)

ABSTRACT

This work reports the fabrication of polydopamine-functionalized mesoporous silica ($mSiO_2$/PDA) nanospheres for removing U(VI) from aqueous solution. The maximum adsorption capacity of $mSiO_2$/PDA is 332.3 mg/g at 318.15 K and pH = 5.5. In comparison to the pristine $mSiO_2$, the adsorption capacity of $mSiO_2$/PDA has been remarkably enhanced, which can be ascribed to the large amounts of functional groups existed on the surface of $mSiO_2$/PDA. The adsorption process fits well with the pseudo-second-order kinetics model. The adsorption isotherm follows the Langmuir isotherm model, revealing a monolayer adsorption of U(VI) onto $mSiO_2$/PDA. Thermodynamic analysis indicates a spontaneous and endothermic adsorption process. Additionally, this adsorption process is pH-dependent, while the effect of ionic strength is negligible.

1. Introduction

Currently, nuclear power is wildly developed in the world because it is an economical and reliable energy without the emission of greenhouse gases [1,2]. Whereas, large amounts of radioactive waste water has been released into environment from the fuels cycles including mining, processing and spent fuels reprocessing activities [3,4]. Uranium (U), as a primary raw material for the nuclear reactor, can cause a serious environmental pollution and threaten to human health due to its radioactivity and high toxicity [5]. U usually exists in the environment in the hexavalent form (U(VI)), such as radioactive UO_2^{2+} ions [6], and it is difficult to be degraded in water [7]. Therefore, much attention should be paid to develop high efficient and selective technologies to remove U(VI) from aqueous solutions. Several approaches, including adsorption, ion exchange, chemical precipitation, membrane filtration, electrodialysis and biological processes have been developed to exclude U(VI) from waste water [6,8–13]. Among them, the adsorption technology is one of the most favorite choices because of its unique merits, such as easy operation, economical feasibility, low cost, etc. [14–18]. Various adsorbents, such as carbon materials [19,20], functionalized clay [21], zeolites [22,23], etc. have been applied for the removal of U(VI). However, low adsorption capacities, restricted adsorption conditions and inconvenient separation limited their practical applications. As a result, it is necessary to synthesize new adsorbents with high adsorption capacity for widespread applications in radionuclides treatment.

Recently, mesoporous materials have drawn a great deal of attention for radionuclide removal owing to its excellent identities such as high surface areas, favorable porous structures, remarkable mechanical/thermal stability, and high adsorption capacities [7,24–28]. The mesoporous SiO_2 ($mSiO_2$) is a hopeful candidate for adsorption with superior chemical/mechanical/thermal stability, easy fabrication and modification, low toxicity and good biocompatibility. Due to the large pore size in $mSiO_2$, a high capacity for UO_2^{2+} entrapment was achieved compared to homologous microporous materials [29]. Nevertheless, owing to the lack of active sites on the adsorbent's surface, the adsorption selectivity and capacity of pure $mSiO_2$ were still confined. To solve this problem, Zhao et al. [30] functionalized $mSiO_2$ with amidoxime for the removal of U(VI), because of the high ability of amidoxime forming complexes with U(VI) ions. Similarly, the carboxymethylated polyethyleneimine (CMPEI) was also grafted on to the surface of ordered $mSiO_2$ (MSU-H) substrate and the CMPEI/MSU-H presented a high adsorption

* Corresponding authors.
E-mail addresses: jiangwq@ustc.edu.cn (W. Jiang), gongxl@ustc.edu.cn (X. Gong), xuansh@ustc.edu.cn (S. Xuan).

http://dx.doi.org/10.1016/j.apsusc.2017.07.274
0169-4332/

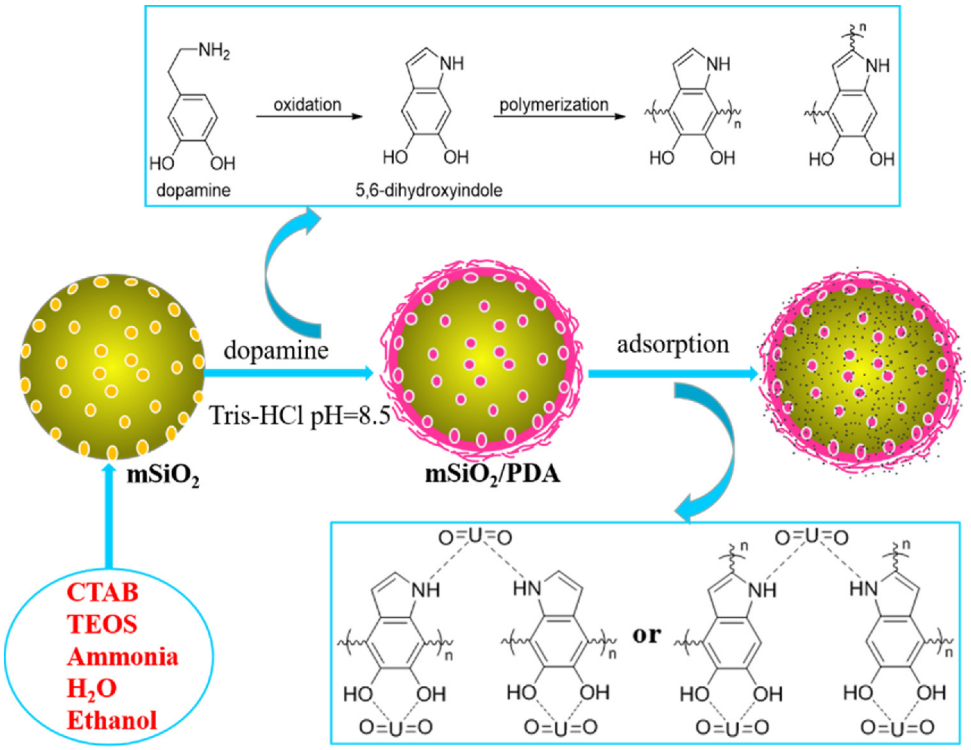

Fig. 1. The mechanism and illustration of the synthesis of $mSiO_2$/PDA nanospheres and the mechanism of U(VI) adsorption on $mSiO_2$/PDA surfaces.

capacity (153 mg/g) and a significantly high U loading stability [31]. More recently, Yuan et al. [32] grafted the phosphonate on $mSiO_2$ for U(VI) adsorption. Owing to the strong complexation between the phosphoryl group and U(VI), a high performance on solid-phase extraction and enrichment of U(VI) was obtained. Therefore, it is quite meaningful to develop a simple, mild and eco-friendly surface modification method for improving the adsorption capacity and efficiency of $mSiO_2$.

Dopamine, as an adhesive protein excreted by marine mussels, has attracted increasing attention because it exhibits remarkable performance in adhesion onto the surface of both organic and inorganic substrates by self-polymerizing to PDA under alkalescent condition [33–37]. Most importantly, the PDA owns abundant catechol and amine groups which could exhibit an extraordinarily admirable ability to bind metal ions via hydrogen bonding, chelating, or bridged bidentate bonding interaction [38,39]. However, the PDA is very easy to form aggregation during the preparation of the micro or nanometer particles. The decrease of PDA dispersibility reduces the surface areas and limits its practical application in adsorption. Therefore, many researchers have been focused on coating PDA on the nanomaterials so as to reduce its aggregation and increase its specific surface area [40,41]. Due to their unique structure characteristics, the final nanocomposites have been widely applied in adsorption, drug delivery, catalysis, and biomimetics [34,38,40–43]. In consideration of the large surface area, the functionalizing of $mSiO_2$ with high reactive PDA will be an eco-friendly and effective way in treating radioactive toxic pollutants. It was reported that the coating of PDA on the surface of $mSiO_2$ could improve the drug loading and releasing capacity. The $mSiO_2$/PDA core/shell nanopsheres also have been proven to be effective for treating cadmium and methylene blue pollution [44–47]. However, the development of high performance $mSiO_2$/PDA nanospheres toward U(VI) removal has not been reported. Moreover, the detailed investigation of its removing mechanism is very important for not only fundamental study but also practical applications.

In this work, a facile approach is developed to synthesize PDA functionalized $mSiO_2$ nanopsheres. Due to its excellent adsorption capacity and adsorption efficiency, $mSiO_2$/PDA exhibits potential applications in U(VI) removal. The adsorption performance of $mSiO_2$/PDA for U(VI) is evaluated by passel adsorption techniques under a variety of conditions such as contact time, temperature, pH value and ionic strength. The adsorption kinetic and isothermal studies are utilized to understand the possible adsorption mechanism. Furthermore, the $mSiO_2$/PDA possesses much higher adsorption capacity and adsorption efficiency than $mSiO_2$ and other adsorbents, which shows great potential for U(VI) removal in practical applications.

2. Experimental section

2.1. Materials

Hexadecyl trimethyl ammonium Bromide (CTAB), tetraethoxysilane (TEOS), ammonia hydroxide (NH_4OH, 25–28%), ethanol (EtOH), trihydroxymethyl aminomethane (Tris), and hydrochloric acid (HCl) were purchased from Sinopharm Chemical Reagent Co. Ltd(SCRC). 3-hydroxytyramine hydrochloride (DA-HCl) was purchased from Aladdin. The UO_2^{2+} stock solution (1.0 mmol/L) was obtained from its nitrate (99.9%, Sigma–Aldrich) after dissolution and dilution with 0.01 mol/L HNO_3 solution. They were all reagent-grade chemicals and used without further purification. Deionized water was utilized for experiment.

2.2. Synthesis of PDA-modified mesoporous Silica ($mSiO_2$/PDA)

Firstly, the mesoporous silica nanospheres were prepared on the basis of ordinary method [48]. Typically, 688 mg of CTAB, 17.2 mL of water, 2.28 mL of ethanol and 35 μL of ammonia hydroxide were mixed and stirred in oil bath at 348.15 K for 30 min. Afterwards, 1.6 mL of TEOS was injected into the mixture slowly and stirred for further 2 h. The as-synthesized milk-white suspension was cooled

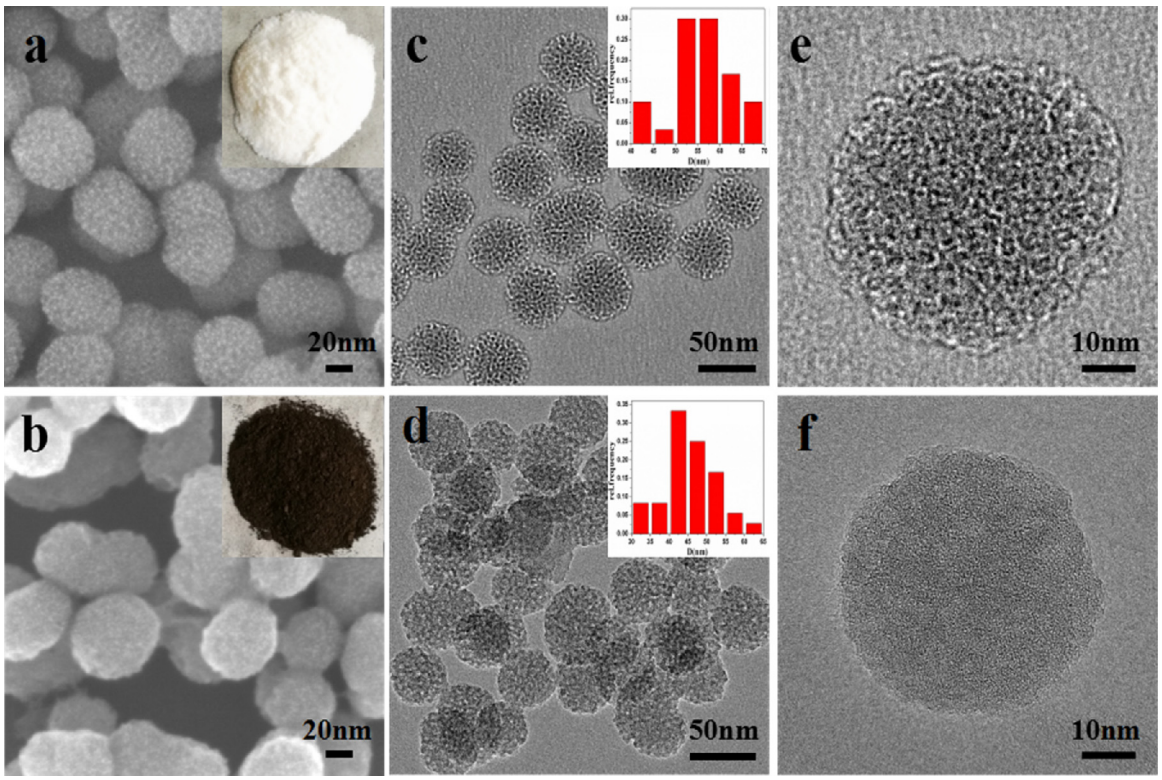

Fig. 2. SEM images of the $mSiO_2$ (a) and $mSiO_2$/PDA (b) nanospheres. Inset: photographs of the $mSiO_2$ (a) and $mSiO_2$/PDA (b) nanospheres. TEM images of the $mSiO_2$ (c, e) and $mSiO_2$/PDA (d, f) nanospheres. Inset: size distribution of the $mSiO_2$ (c) and $mSiO_2$/PDA (d) nanospheres.

to room temperature and isolated by centrifugation in ethanol. The templates were removed through ultrasonication in ethanol and hydrochloric acid mixture solution for 30 min. Then, in order to prepare PDA modified $mSiO_2$, 20 mg as-prepared $mSiO_2$ nanospheres were dispersed in a mixture of 20 mL Tris-HCl (PH = 8.5) and 40 mL ethanol. 20 mL DA-HCl aqueous solution (4 mg/mL) was added into the reaction mixture and continuously stirred for 24 h at room temperature. Finally, the resultant $mSiO_2$/PDA nanospheres were separated by centrifugation and washed three times with ethanol, and dried in vacuum oven at 323.15 K.

2.3. Characterization

The size and morphology were investigated by the field emission transmission electronic microscopy (FETEM, JEM-2100F) with an accelerating voltage of 200 kV, and the field emission scanning electron microscope (FESEM, JEM-500, 20 kV). The Nitrogen adsorption isotherms were measured with N_2 adsorption–desorption measurements (Tristar II 3020 M). X-ray photoelectron spectra (XPS) were conducted on an ESCALAB 250. Thermogravimetric (TG) analysis was performed on a DTG-60H thermogravimetric instrument under the atmosphere of air from room temperature to 973.15 K at the rate of 10 K/min. Infrared (IR) spectra were recorded with a TENSOR Model 27 Fourier transform infrared (FT-IR) spectrometer in the wave number range 4000–400 cm^{-1} using a KBr wafer. The Raman spectra of the samples were acquired by confocal laser micro Raman spectrometer. Zeta potential was tested by Zeatsizer Nano ZS (Malvern, England).

2.4. Adsorption experiment

The batch experiments of U(VI) adsorption on $mSiO_2$ and $mSiO_2$/PDA were investigated in polyethylene test tubes (10 mL). The U(VI) stock solution (60 mg/L), $NaNO_3$ solution (1 mol/L), adsorbent stock solution (1 g/L) and Milli-Q water were mixed in test tubes with desired concentrations of different components. The effects of ionic strength are studied in the presence of $NaNO_3$ solution with concentrations of 0.001, 0.01, 0.1 mol/L. The solution pH was adjusted by adding negligible amount of 0.1 mol/L NaOH or 0.1 mol/L HNO_3 solution. Then the tubes were put in an oscillator and kept shaking for a desired time. The adsorbent was separated by centrifugation at 8000 r/min for 15 min, and the concentration of U(VI) in supernatants was measured by the Dichlor-ophosphonoazo III Spectrophotometer (V-1600 Mapada Shanghai) method at the wavelength of 669 nm. The adsorption capacities (q_e) of U(VI) on $mSiO_2$ and $mSiO_2$/PDA were calculated from the different initial concentration (C_o) and the equilibrium concentration (C_e), and the mass balance equation as follow is used to express adsorption properties.

$$q_e = \frac{(C_0 - C_e) \times V}{m}$$

Where V (L) is the total volume of the suspension, and m (g) is the mass of adsorbent. All the experimental data were the average of duplicate determinations and the relative errors were within 5%. In this experiment, the contact time, temperature, solution pH and ionic strength were used to investigate the adsorption performance of $mSiO_2$ and $mSiO_2$/PDA.

3. Results and discussion

3.1. Synthesis and characterization of $mSiO_2$/PDA nanospheres

Fig. 1 illustrated the synthesis process of the $mSiO_2$/PDA. Firstly, monodispersed $mSiO_2$ nanospheres with average particle size ~55 nm were synthesized by a modified Stöber reaction. After the CATB templates were removed through ultrasonication in ethanol and hydrochloric acid mixture solution, $mSiO_2$ nanospheres with

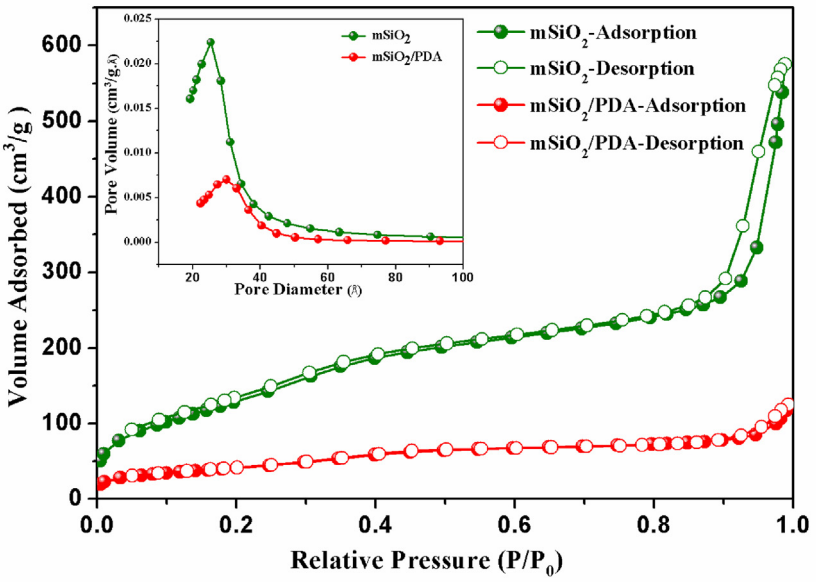

Fig. 3. Nitrogen adsorption-desorption isotherm and Barrett–Joyner–Halenda (BJH) pore size distribution plot (inset) of $mSiO_2$ and $mSiO_2$/PDA nanospheres.

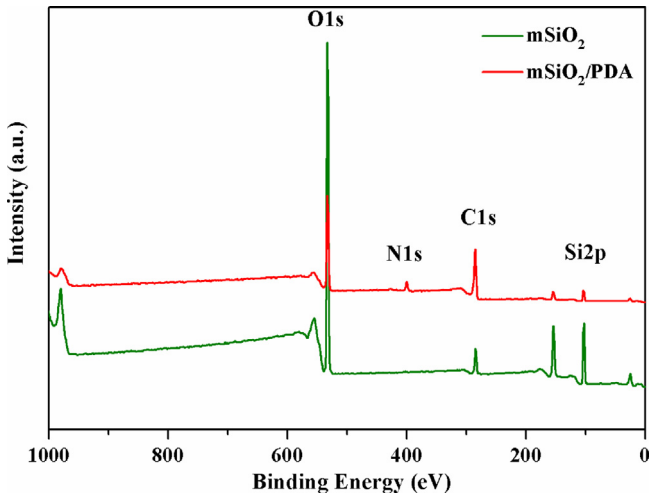

Fig. 4. Broad-range XPS spectra of $mSiO_2$ and $mSiO_2$/PDA nanospheres.

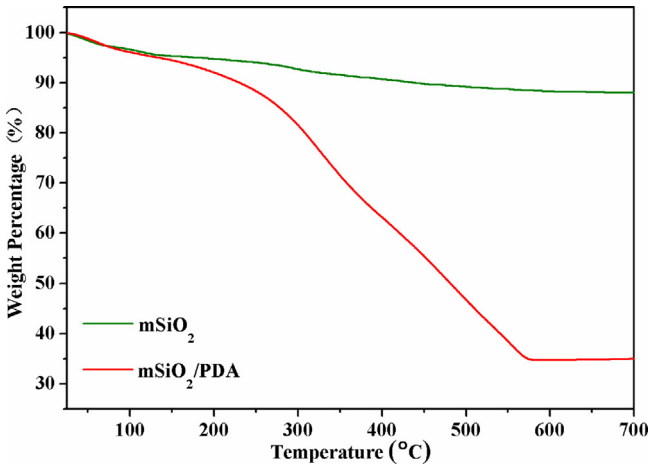

Fig. 5. TG curves of the as prepared $mSiO_2$ and $mSiO_2$/PDA nanospheres.

favorable porous structures were obtained. Then, as-prepared $mSiO_2$ nanospheres were dispersed in Tris-HCl (pH = 8.5) solution and the dopamine was added into the reaction mixture to functionalize the surface of the $mSiO_2$ nanospheres. During the polymerization, the dopamine favored to attach on the solid substrate, in which the H-bonds played an important role in formation of $mSiO_2$/PDA [49]. After the final products ($mSiO_2$/PDA) were obtained, they were used to absorb U(VI) from aqueous solution.

Fig. 2a and b show the SEM images of $mSiO_2$ and $mSiO_2$/PDA nanospheres, respectively. It was obvious that nanospheres presented a spherical morphology while a small fraction of nanospheres exhibited irregular morphology. Additionally, all the nanospheres were well dispersed without any large-scale conglomeration. In comparison to $mSiO_2$ nanospheres, $mSiO_2$/PDA had a rougher surface, suggested the presence of a thin layer coating on the surface of the $mSiO_2$. The monodispersity and morphology of the prepared samples can also be clearly observed from the TEM images. As shown in Fig. 2c, $mSiO_2$ nanospheres were uniform and the diameter was 55 ± 10 nm. The TEM images of $mSiO_2$/PDA nanospheres were presented in Fig. 2d with the diameter of 45 ± 10 nm and the size distribution of the $mSiO_2$ and $mSiO_2$/PDA nanospheres were shown in the insets of Fig. 2c and d, respectively. The average diameter of $mSiO_2$/PDA nanospheres were slightly smaller than $mSiO_2$, which because the reaction were conducted in the Tris-HCl (pH = 8.5) buffer solution. During the reaction, the $mSiO_2$ particles were slightly dissolved in the alkaline medium, while the additional PDA shell was very thin. Therefore, the average diameter of $mSiO_2$/PDA nanospheres was slightly smaller than $mSiO_2$. The inner nanostructure can be clearly observed by high magnification TEM images. As shown in Fig. 2e, there were obvious porous structures inside the $mSiO_2$ nanospheres. In the TEM images of $mSiO_2$/PDA (Fig. 2f), the pores were significant reduced due to the coating of PDA on the $mSiO_2$ surface, which agreed well with the SEM analysis. Due to the low contrast, it is very difficult to distinguish the PDA layer from the $mSiO_2$. However, the color of $mSiO_2$ changed from white to dark brown after the dopamine coating (the insets of Fig. 2a and b), which also demonstrated that the $mSiO_2$ nanospheres were successfully functionalized by the PDA layer. Here, it is estimated that the PDA not only forms a thin layer on the periphery of the $mSiO_2$ nanospheres but also attached onto the inner surface of the nanopores. Moreover, since the amor-

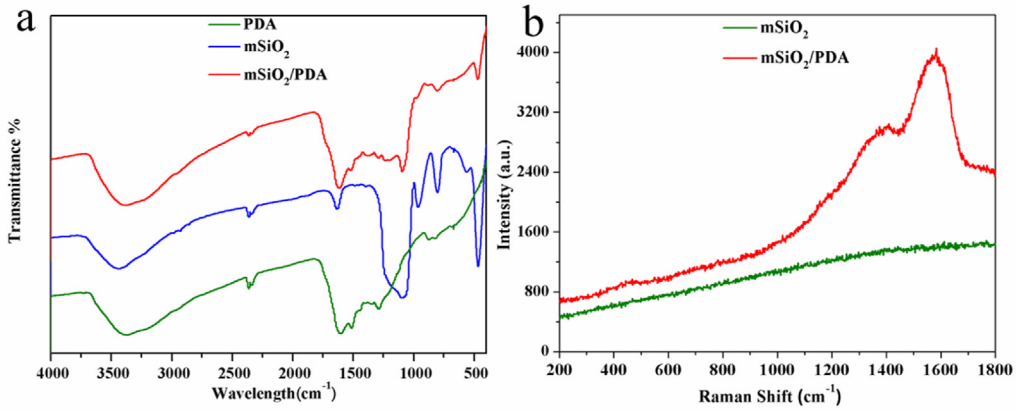

Fig. 6. FTIR spectra (a) of PDA, $mSiO_2$ and $mSiO_2$/PDA and Raman spectra (b) of $mSiO_2$ and $mSiO_2$/PDA.

phous nature of the $mSiO_2$, only a broad peak was found in the XRD pattern (Fig. S2). After the modification with PDA, no other distinctive peak was determined in $mSiO_2$/PDA, which revealed the low crystallization of the final $mSiO_2$/PDA nanospheres.

Brunauer-Emmett-Teller (BET) measurements were conducted to investigate the differences between $mSiO_2$ and $mSiO_2$/PDA. Fig. 3 shows the nitrogen adsorption-desorption isotherm curves and the pore size distribution curves of the synthesized $mSiO_2$ and $mSiO_2$/PDA nanospheres. It can be distinctly observed that $mSiO_2$ showed typical IV-type isotherm and H1-type hysteresis loops. The isotherm changed clearly after $mSiO_2$ modification with PDA. From Fig. S1, it is found that the isotherm had a small hysteresis loop. The reason for this may be attributed to the pores with diameters smaller than 4 nm [50]. The similar result can be observed from the inset in Fig. 3. The pore size distribution curve of $mSiO_2$/PDA has an obvious peak in mesopore region, indicating the presence of mesoporous structure in $mSiO_2$/PDA. Therefore, the isotherm for $mSiO_2$/PDA can be assigned to type IV according to the IUPAC classification. Obviously, the nitrogen adsorption capacity decreased after being decorated with PDA. As can be seen from Table S1, the mean pore size of $mSiO_2$/PDA (4.0 nm) was smaller than pristine $mSiO_2$ (5.3 nm). Furthermore, the decrease in the BET surface area (from 506.1 to 135.4 m^2/g) and the pore volume (from 0.67 to 0.14 m^3/g) of $mSiO_2$/PDA are due to the decoration of PDA inside the channels but not totally blocked with PDA.

X-ray photoelectron spectroscopy (XPS) was employed to analyze the surface state of the final product. As shown in Fig. 4, strong O1s and Si2p characteristic peaks appear in the $mSiO_2$ spectrum. The tiny C1s peak in the spectrum is attributed to the residual ethanol or $-OCH_2CH_3$ groups on the surface of the $mSiO_2$. For the $mSiO_2$/PDA, a characteristic nitrogen signal can be easily seen and there is about 9.0% (molar ratio) of nitrogen (N1s, 401 eV) on the surface of the $mSiO_2$/PDA. Furthermore, compared with $mSiO_2$, the signal of Si still exists and the intensity of Si peak reduces in $mSiO_2$/PDA, indicating that PDA is successfully covered on $mSiO_2$ surface and the thickness of the polymer coating is thinner than the detective depth of the XPS (10 nm). These results prove the successful coating of PDA onto $mSiO_2$ because the PDA contains huge amounts of aromatic rings and amide and catechol functional groups, which leads to the enhancement of N1s and C1s signals in the XPS spectra.

The thermogravimetric curves of the as-prepared samples are shown in Fig. 5. The weight loss process was tested between 298.15 and 973.15 K. The curves of Fig. 5 present the weight loss process of $mSiO_2$ and the trifling weight loss from 298.15 to 373.15 K is due to adsorbed water. With the temperature increasing, the observed inconspicuous weight loss can be responded for the residual organic groups in the $mSiO_2$ nanospheres, which is consistent with the XPS analysis. Furthermore, siloxane bridges were formed with expulsion of water molecules between 473.25 K and 873.15 K. For $mSiO_2$/PDA, the weight decreases remarkably when the temperature rising to more than 473.15 K, which can be ascribed to the decomposition of PDA. The final weight loss of $mSiO_2$ and $mSiO_2$/PDA are 12.1% and 65.0%, respectively. Therefore, the weight loss of $mSiO_2$/PDA is higher than $mSiO_2$ which indicates that PDA modified the $mSiO_2$ successfully.

The FTIR and Raman spectra of the samples synthesized in each step were investigated (Fig. 6). The distinctive adsorption peaks of $mSiO_2$ are found at 800 cm^{-1}, 1090 cm^{-1}, 469 cm^{-1}, which are attributed to the asymmetric stretching vibration ν_s (Si—O—Si), the asymmetric stretching vibration ν_{as} (Si—O—Si) and the Si—O—Si bending mode. Moreover, the 3440 cm^{-1} and 957 cm^{-1} are the typical peaks for Si-OH stretching vibration. The characteristic absorption peaks of PDA are approximately located at 3440 cm^{-1} (phenolic O—H and N—H stretching vibration), 1620 cm^{-1} (N—H bending vibration and aromatic ring stretching vibration), 1510 cm^{-1} (N—H shearing vibration), and 1090 cm^{-1} (C—O vibration). All of the above absorption peaks can be found in the spectrum of $mSiO_2$/PDA, which indicates that the $mSiO_2$ is successfully modified with the polymerized dopamine. In Raman spectra (Fig. 6b), the obvious peaks at 1584 cm^{-1} and 1409 cm^{-1} are attributed to the stretching and deformation of aromatic rings, which are originated from the PDA.

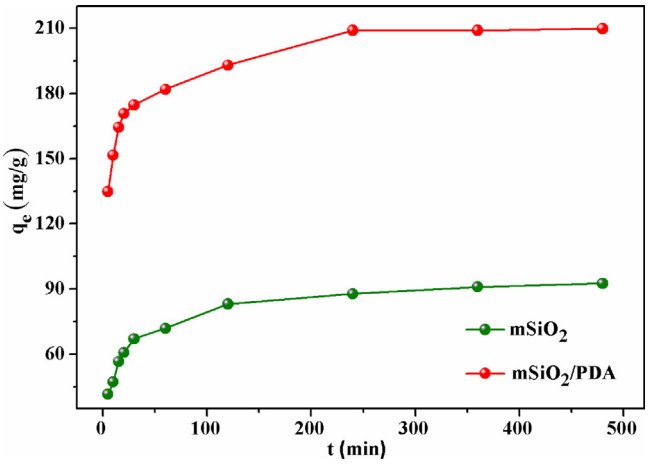

Fig. 7. The effect of contact time on the adsorption of U(VI) onto $mSiO_2$ and $mSiO_2$/PDA, T = 298.15 K, pH = 5.5 ±0.1, $C_{U(VI)(original)}$ = 33 mg/L, m/V = 1 g/L.

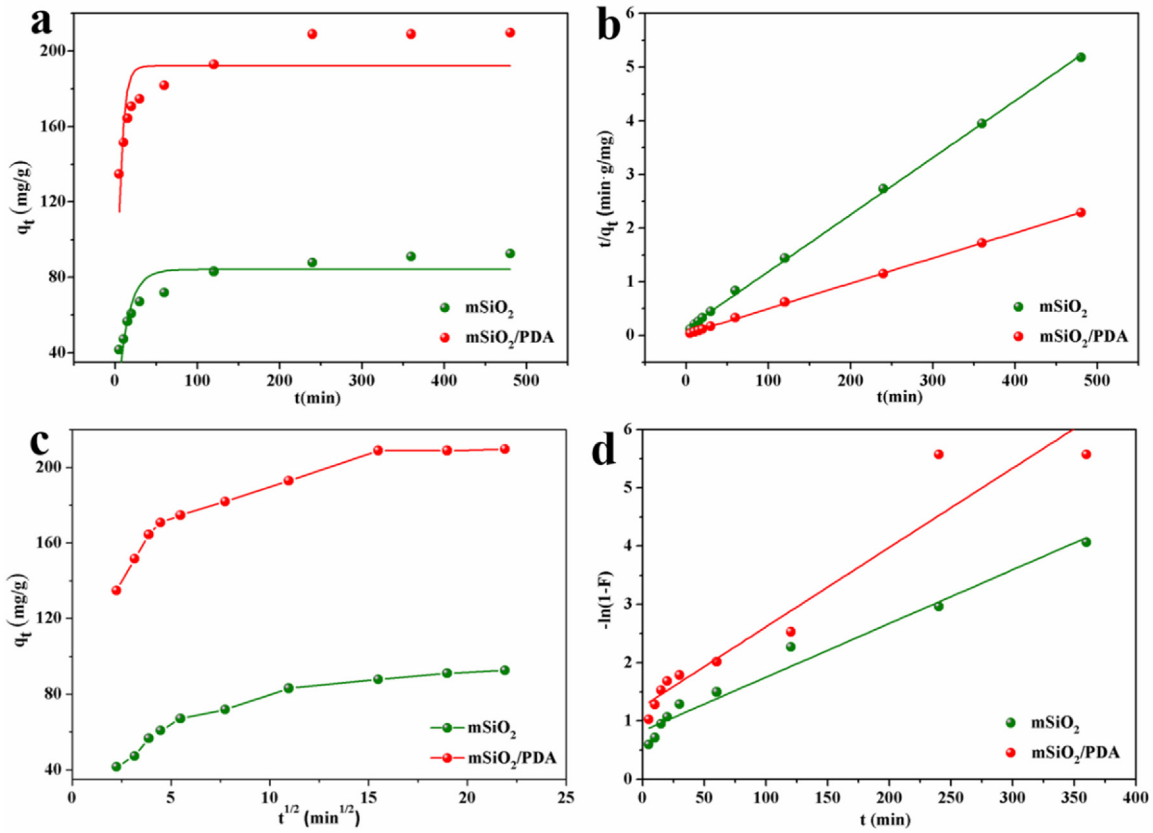

Fig. 8. Adsorption kinetics of U(VI) on $mSiO_2$ and $mSiO_2$/PDA surface (a) pseudo-first-order, (b) pseudo-second-order, (c) intra-particle diffusion, (d) Boyd. T = 298.15 K, pH = 5.5 ± 0.1, $C_{U(VI)(original)}$ = 33 mg/L, m/V = 1 g/L.

Table 1
Parameters for different kinetic models.

Model	$mSiO_2$			$mSiO_2$/PDA		
Pseudo-first-order	k_1 (min^{-1})	q_e (mg/g)	R^2	k_1 (min^{-1})	q_e (mg/g)	R^2
	0.077	84	0.7818	0.1817	192	0.5737
Pseudo-second-order	K_2 (g/mg min)	q_e (mg/g)	R^2	K_2 (g/mg min)	q_e (mg/g)	R^2
	4.38E-04	94	0.9994	3.99E-04	212	0.9997

3.2. Adsorption kinetics

The effect of time on the adsorption of U(VI) onto $mSiO_2$ and $mSiO_2$/PDA was performed with adsorbent concentration of 1 g/L at 298.15 K (Fig. 7). The adsorption of U(VI) is fast in the first 30 min, and then reaches equilibrium slowly with extending contact time. This adsorption characteristic is mainly due to the higher concentration of U(VI) in the solution and abundance of active sites on the surface of adsorbent at the beginning of adsorption. Besides, it is obvious that the maximum adsorption capacity of $mSiO_2$/PDA nanospheres (209.8 mg/g) is much higher than $mSiO_2$ (92.6 mg/g), which benefits from the modification of PDA on the $mSiO_2$ surface. The relatively fast adsorption rate and high adsorption capacity indicate that $mSiO_2$/PDA has outstanding potential for practical application in removing U(VI) from wastewater. According to the experimental results, it is more efficient to reach adsorption equilibrium within 4 h when compared with other adsorbents [29,49–53]. Therefore, the adsorption time of 4 h is set in subsequent experiments.

To further investigate the adsorption behavior of U(VI) on $mSiO_2$ and $mSiO_2$/PDA surface, the experimental data are analyzed with four kinetic models including the pseudo-first-order, pseudo-second-order, intra-particle diffusion, Boyd kinetic models. Eq. (1) shows the pseudo-first-order kinetic model [54]:

$$q_t = q_e(1 - e^{-k_1 t}) \quad (1)$$

Where k_1 (min^{-1}) is the pseudo-first-order kinetic rate constant, and q_e (mg/g) and q_t (mg/g) represent the amount of U(VI) adsorbed on adsorbents at equilibrium and at time t, respectively. The values of k_1 and q_e are calculated from Fig. 8a and the results are presented in Table 1. The values of correlation coefficient (R^2) for $mSiO_2$ and $mSiO_2$/PDA are 0.7818 and 0.5737, respectively. The relatively low values of R^2 indicate that the pseudo-first-order kinetic model is not fit for analyzing the adsorption process.

The pseudo-second-order kinetic model also used to characterize the adsorption behavior, which is based on the assumption that the adsorption rate is controlled by the chemical adsorption mechanism. In this model, the rate of U(VI) removal with time is proportional to the square of the driving force. The linear form of the equation is exhibited as follows [55]:

$$\frac{t}{q_t} = \frac{1}{k_2 q_e^2} + \frac{1}{q_e} t \quad (2)$$

Table 2
The U(VI) adsorbability of $mSiO_2$/PDA compared with other sorbents.

Material	Q_m (mg/g)	Experiment conditions	Reference
PGO	251.7	pH = 5.5 ± 0.1	8
polyacrylamide coated-Fe_3O_4	220.9	pH = 5.0	61
CMPEI/MSU-H	153	pH = 9.5	31
phosphonate-functionalized mesoporous silica	303	pH = 6.9 ± 0.2	32
dihydroimidazole –functionalized SBA-15	268	pH = 5.0 ± 0.1	62
$mSiO_2$/PDA	332.3	pH = 5.5 ± 0.1	this work

Where k_2 (g/mg min) is the pseudo-second-order rate constant. The values of kinetic parameters q_e and k_2 are acquired by plotting t/qt versus t (Fig. 8b and Table 1). The R^2 for the pseudo-second-order kinetic model of $mSiO_2$ and $mSiO_2$/PDA reaches up to 0.9994 and 0.9997, respectively, which means that the pseudo-second-order kinetic model can explain this adsorption process well and the adsorption processes on $mSiO_2$ and $mSiO_2$/PDA surfaces are similar. These results indicate that the pseudo-second-order is the dominant mechanism and U(VI) adsorption on adsorbent surface is the chemisorption process. It is also suggested that the rate-controlling step may be chemical adsorption and chemisorption might involve the valency forces through sharing electrons between adsorbents and U(VI) ions [52].

In consideration of the intra-particle diffusion in adsorption process, the intra-particle diffusion model is applied to simulate the adsorption behavior. This kinetic model is usually used to analyze the controlling steps of reaction, which assumes that the diffusion rate of U(VI) is the controlling step of adsorption process and the intra-particle diffusivity is invariable [56,57]. The intra-particle diffusion rate equation is depicted as follow [58]:

$$q_t = k_i t^{1/2} + C \quad (3)$$

Where k_i is the intra-particle diffusion rate constant and C represents the influence of boundary layer. The plot of q_t versus $t^{1/2}$ is shown in Fig. 8c. If the plot is a straight line and passes through the origin, the intra-particle diffusion is the single rate determining step in adsorption process [59]. From Fig. 8c, the experimental curves consists of three different straight lines suggesting that there are over one controlling stages in adsorption process. The original straight line is corresponding to the external surface adsorption, of which the U(VI) in solution diffuses to the external surface of adsorbent. A gradual adsorption in the second linear portion is related to intra-particle diffusion of U(VI) ions through the pores of adsorbent. The last line is the final equilibrium stage and the intra-particle diffusion starts to slow down because of the low concentration of U(VI) remaining in the solution phase and the reduction of active sites. Moreover, the three straight lines in the plot all cannot pass through the origin, indicating that the intra-particle diffusion has significant influence on the rate determination in adsorption process but not the only rate determining factor. Thus, it can be concluded that film diffusion and intra-particle diffusion are the rate determining step of the adsorption process simultaneously. In addition, $mSiO_2$/PDA with higher density of organic groups, smaller surface area and fewer mesoporous structures are expected to exhibit slower adsorption rate due to stronger steric constraints. However, as shown in Fig. 8c, the whole adsorption rate of U(VI) onto the $mSiO_2$/PDA is faster than that onto $mSiO_2$, indicating that not only pore structure but also the number of active sites affect the adsorption kinetics. Since there are abundant amide and catechol functional groups on the surface and inner pores of $mSiO_2$/PDA which can combine with U(VI), the $mSiO_2$/PDA shows much faster adsorption rate and higher adsorption capability.

Further, the Boyd kinetics model is a sole-resistance model which is applied to analyze the actual rate determining step in adsorption process and assumes that the major adsorption resistance is concentrated on the adsorbent particle boundary layer. The equation is expressed as follows [7,60]:

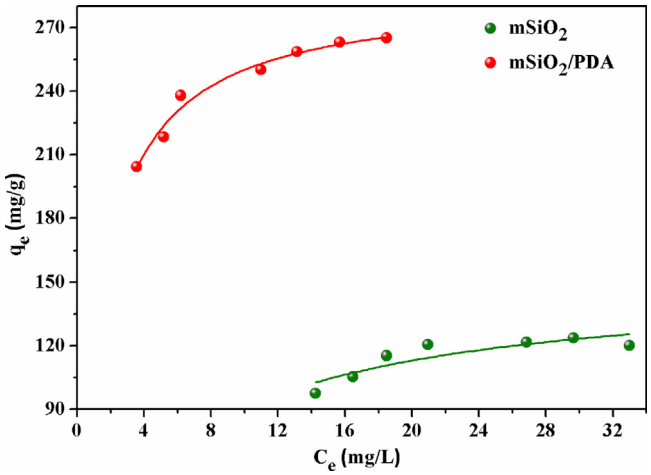

Fig. 9. Adsorption isotherms of U(VI) onto $mSiO_2$ and $mSiO_2$/PDA. T = 298.15 K, pH = 5.5 ± 0.1, m/V = 1 g/L.

$$\ln(1 - F) = -k_f t \quad (4)$$

Where k_f is the film diffusion rate constant and F is the fractional attainment of equilibrium at different time t, and the equation is given as:

$$F = \frac{q_t}{q_e} \quad (5)$$

The Fig. 8d shows the line by plotting *-ln(1-F)* against *t*, and introduce to differentiate between the film diffusion and intra-particle diffusion. If the plot is a straight line and passes through the origin, the adsorption rate is controlled by intra-particle diffusion, if not, the film diffusion or chemical reaction limits the adsorption rate. The line in Fig. 8d also cannot pass through the origin, indicating that the film diffusion is the primary rate controlling step for removing U(VI), which is consistent with the consequence from intra-particle diffusion model well.

3.3. Adsorption isotherms

Fig. 9 shows the adsorption isotherms of U(VI) on the $mSiO_2$ and $mSiO_2$/PDA at various U(VI) concentrations, which clearly demonstrates the effect of the initial concentration of U(VI) on the adsorption capacity of adsorbent. The adsorption isotherms of $mSiO_2$ and $mSiO_2$/PDA are acquired under the equal conditions to compare their adsorption capacity. As presented in Fig. 9, with the increasing of U(VI) concentrations, the adsorption capacity of U(VI) increases when the equilibrium state of the adsorption process is attained. Furthermore, it is obvious that the adsorption capacity of $mSiO_2$/PDA to U(VI) is much larger than $mSiO_2$ under the same conditions. The maximum adsorption capacities of $mSiO_2$/PDA and $mSiO_2$ are 286.5 mg/g and 150.8 mg/g at 298.15 K, respectively. The experimental results indicate that the $mSiO_2$/PDA exhibits

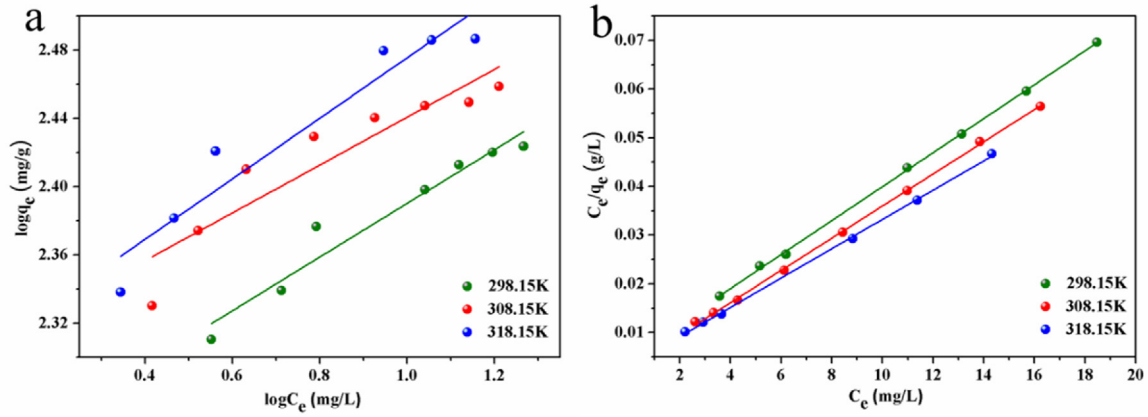

Fig. 10. Linear plots of Langmuir model (a), Freundlich model (b) for U(VI) adsorption by $mSiO_2$/PDA at different temperatures.

enhanced adsorption performance compared with the undecorated $mSiO_2$, which can be ascribed to large amounts of functional groups on the surface of $mSiO_2$/PDA. It is worthy to mention that $mSiO_2$/PDA exhibits much higher ability of U(VI) removal compared with other sorbents. Table 2 shows the maximum adsorption capacity (Q_m) of U(VI) on $mSiO_2$/PDA and other previous reported adsorbents, which was calculated from Langmuir isotherm model. In conclusion, the $mSiO_2$/PDA has excellent adsorption capacity for U(VI) and the maximum capacity (Q_m) is 332.3 mg/g at 318.15 K.

For the purpose of exploring the adsorption behavior of $mSiO_2$/PDA, the Langmuir and Freundlich adsorption models are applied to analyze the experimental data. The Langmuir model, based on the assumption of monolayer adsorption process and all binding sites having same adsorption affinity, is widely used to simulate the adsorption process in previous literatures. The linearly form equation of the Langmuir model is expressed as follows [54,63]:

$$\frac{C_e}{q_e} = \frac{1}{Q_m K_L} + \frac{1}{Q_m} C_e \quad (6)$$

Where C_e is the final concentration of U(VI) in aqueous solution (mg/L), q_e is the amount of U(VI) adsorbed on the adsorbent (mg/g), Q_m is the maximum adsorption capacity (mg/g) and K_L is the Langmuir constant (L/mg) relating to adsorption intensity. As presented in Fig. 10a, the straight lines are acquired by plotting C_e/q_e against C_e and the values of Q_m and K_L can be calculated from the intercept and slope of the line.

The Freundlich isotherm model emphasized heterogeneity of adsorption surface, non-ideal and multilayer adsorption process. The formula of Freundlich model is expressed as follows [54,64]:

$$\log q_e = \log K_F + n \log C_e \quad (7)$$

Where K_F ($mg^{1-n}\,L^n/g$) and n are Freundlich model contants related to the adsorption capacity and adsorption intensity, respectively. The values of K_F ($mg^{1-n}\,L^n/g$) and n are obtained from the intercept and slope of the straight line that plot $logq_e$ versus $logC_e$ (Fig. 10b). The parameters of two models are all listed in Table 3. The correlation coefficient (R^2) of Langmuir and Freundlich models clearly indicates that the experiment data can be described properly by the Langmuir model. The consequence indicates that adsorbed U(VI) ions form a monolayer coverage on the surface of $mSiO_2$/PDA and chemisorption is the dominating adsorption mechanism in this adsorption process, which is in keeping with the adsorption kinetics analysis. The main reasons may be the homogeneous distribution of active sites on the surface of $mSiO_2$/PDA and there is no interaction and competition with each other among the adsorbed U(VI) ions. The values of Q_m obtained from Langmuir model are 287.5, 303.0 and 332.3 mg/g at 298.15, 308.15 and 318.15 K, respectively, which indicate that the higher temperatures is beneficial to enhance the adsorption capacities of $mSiO_2$/PDA, confirming an endothermic adsorption process.

Table 3
Parameters for Langmuir and Freundlich adsorption models.

Models	Parameters			
	T (K)	Q_m (mg/g)	K_L (L/mg)	R^2
Langmuir	298.15	287.5	0.687	0.9995
	308.15	303.0	1.122	0.9994
	318.15	332.3	0.953	0.9992
		K_F ($mg^{1-n}\,L^n/g$)	n	R^2
Freundlich	298.15	171.0	0.157	0.9391
	308.15	199.8	0.140	0.8333
	318.15	198.6	0.178	0.9088

In general, larger surface area is beneficial to improve the adsorption capacity of the adsorbents for U(VI) removal. However, compared with $mSiO_2$, $mSiO_2$/PDA exhibits much higher adsorption capacity with lower surface area, demonstrating that the functional groups on the adsorbents surface have significant effect on the adsorption capacity for U(VI) enrichment. The XPS spectra of $mSiO_2$/PDA before and after U(VI) adsorption (expressed as $mSiO_2$/PDA-U(VI)) are presented in Fig. S3. The U(VI) peak presented in the XPS spectrum of the $mSiO_2$/PDA-U(VI) indicates the adsorption of U(VI) on the surface of $mSiO_2$/PDA. To verify the function of active sites, the N1s and O1s peaks of the $mSiO_2$/PDA before and after the adsorption are compared. As shown in Fig. S3b, the intensity of O1s peak decreases distinctly and the peak shifts to higher energy (0.2 eV) after U(VI) adsorption, suggesting that the $mSiO_2$/PDA nanospheres and U(VI) were combined by chemical bonds. Similarly, the intensity and position of N1s (0.25 eV) have a same change after adsorption, revealing that the nitrogen-containing functional groups are significant in the interaction with uranium U(VI) [40]. According to the analysis of XPS and FTIR data, there are large amounts of amide and catechol functional groups on the surfaces of $mSiO_2$/PDA. Based on the previous study, U(VI) ions are linear bonded with two axial oxygen atoms and coordinate with other ligands in the equatorial plane possibly [62]. Therefore, as illustrated in Fig. 1, the mechanisms of $mSiO_2$/PDA interaction with U(VI) ions might be that the amide and catechol functional groups bound to the U center by chemical bond.

3.4. Adsorption thermodynamics

The adsorption thermodynamic studies are used to evaluate the effect of the operating temperature on U(VI) adsorption. The thermodynamic parameters including ΔG^0 (KJ/mol), ΔH^0 (KJ/mol) and

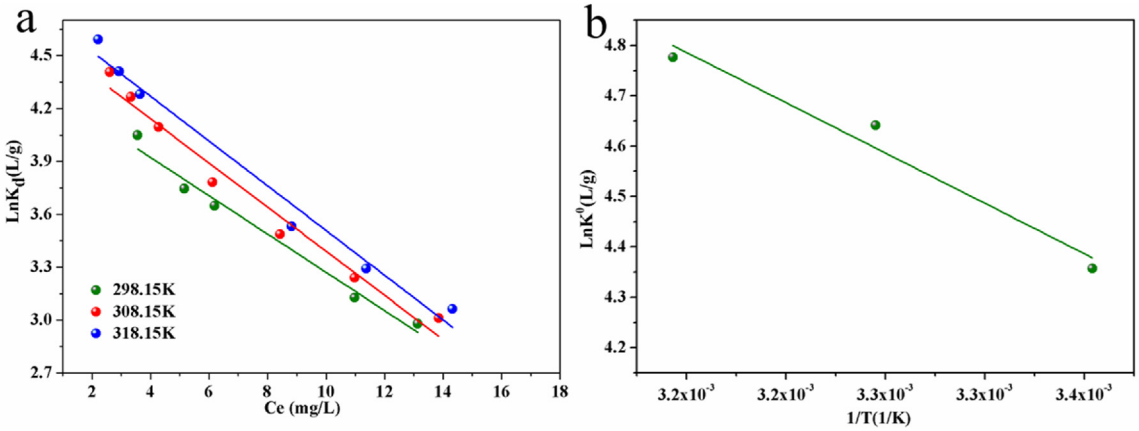

Fig. 11. Linearized plot of lnK_d versus C_e (a) and lnK^0 versus $1/T$ (b).

Table 4
Thermodynamic data for the adsorption of U(VI) on $mSiO_2$/PDA.

T (K)	ΔG^0 (KJ/mol)	ΔH^0 (KJ/mol)	ΔS^0 (J/mol/K)
298.15	−10.81		
308.15	−11.73	16.6	92.1
318.15	−12.65		

ΔS^0 (J/mol/K) could be calculated from the temperature-dependent adsorption isotherms at different test temperatures with the assistance of following formulas [65,66]:

$$K_d = \frac{q_e}{C_e} \quad (8)$$

$$\ln K^0 = \frac{\Delta S^0}{R} - \frac{\Delta H^0}{RT} \quad (9)$$

$$\Delta G^0 = \Delta H^0 - T\Delta S^0 \quad (10)$$

Where R (8.314 J/(mol·K)) is the universal gas constant and T (K) is the temperature in Kelvin. K^0 is the adsorption equilibrium constant which obtained by plotting lnK_d versus C_e (Fig. 11a) and extrapolating C_e to zero.

The change in entropy (ΔS^0) and enthalpy (ΔH^0) are calculated from the intercept and slope of the linear plots of lnK^0 versus $1/T$ (Fig. 11b). The change in Gibbs free energy (ΔG^0) for specific adsorption can be obtained from the thermodynamic Eq. (10). The values of thermodynamic parameters are listed in Table 4. To understand the mechanism of U(VI) removal by $mSiO_2$/PDA well, it is necessary to analyze the thermodynamic parameters. Visibly, the values of ΔG^0 shown in Table 3 are negative, indicating a spontaneous process. And higher temperature is more beneficial to enhance adsorption efficiency due to decreasing values of ΔG^0 with increasing temperature.

Positive ΔH^0 value reveals an endothermic adsorption process, which could be ascribed to the endothermic and recombination process. After adsorption the U(VI) became less aqueous and the process of dehydration is an endothermic process, whereas the recombination of dehydrated U(VI) on $mSiO_2$/PDA is an exothermic process. Higher dehydration process exceeds the recombination process could account for the endothermic adsorption process. In addition, positive ΔS^0 calculated in this adsorption process demonstrates an increased degree of freedom of solute molecules. Overall, the results of thermodynamic parameters indicate that the adsorption process of U(VI) on $mSiO_2$/PDA composite is a spontaneous and endothermic process.

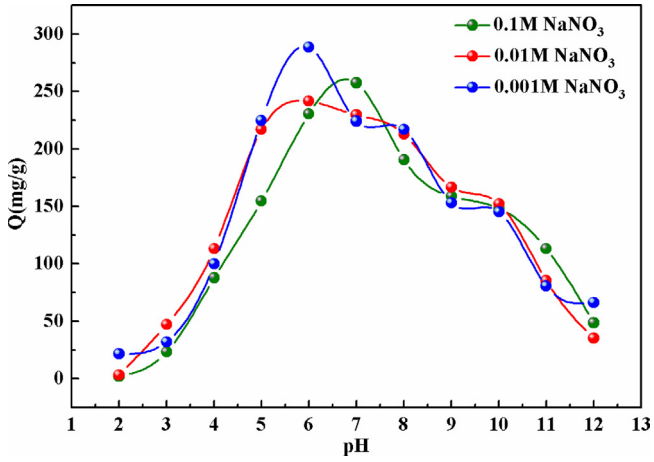

Fig. 12. Effect of pH and ionic strengthon U(VI) adsorption on $mSiO_2$/PDA surface T = 298.15 K, $C_{U(VI)(original)}$ = 33 mg/L, m/V = 1 g/L.

3.5. Effect of pH and ionic strength

The pH of the solution has a remarkable influence on the adsorption of metal ions since the species of U(VI), the surface charge and the active sites of the adsorbents varies at different pH values. The pH effect on removal U(VI) by $mSiO_2$/PDA are investigated with a different initial pH range of 2.0–13.0 at 298.15 K. Fig. 12 presents that the solution pH have impacts on the adsorption of U(VI) on $mSiO_2$/PDA surface. The adsorption capacities of $mSiO_2$/PDA increases dramatically at pH 2.0–6.0, then arrives to the maximum adsorption efficiency when the pH is about 6, nevertheless decreases removal efficiency is observed at pH > 6. Maximum adsorption efficiency is reached at pH 7.0 when the concentration of $NaNO_3$ is 0.1 mol/L, which is different with the other experiment results. Similar adsorption behaviors can be found in some other adsorbents according to previous studies [15,67–69].

The species distributions of U(VI) and the surface properties of $mSiO_2$/PDA vary with pH value, which affects the interactions between U(VI) and $mSiO_2$/PDA, thus the adsorption behavior is pH-dependent. As shown in Fig. 13, at different pH values, U(VI) exists different species including UO_2^{2+}, $UO_2(OH)^+$, $UO_2(OH)_2$, $(UO_2)_3(OH)_5^+$, $(UO_2)_4(OH)_7^+$, $(UO_2)_3(OH)_7^-$, $UO_2(OH)_3^-$ and $UO_2(OH)_4^{2-}$. U(VI) primarily exists as the species of UO_2^{2+} when pH < 5. At pH 5–8, the mixed species of $UO_2(OH)^+$, $(UO_2)_3(OH)_5^+$ and $(UO_2)_4(OH)_7^+$ presents in the solution. Furthermore, the negatively charged species of $(UO_2)_3(OH)_7^-$, $UO_2(OH)_3^-$

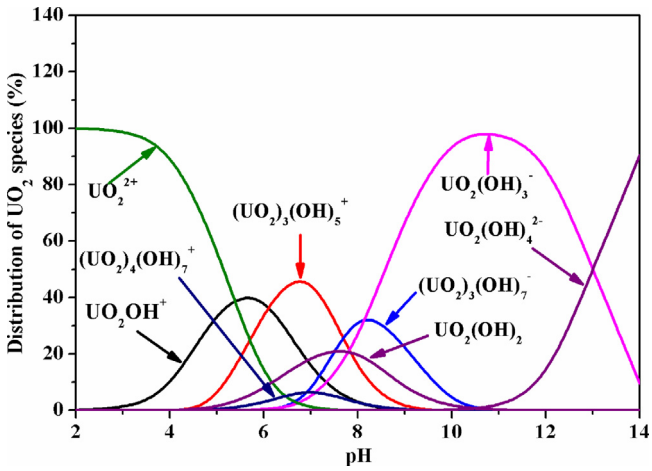

Fig. 13. The species distributions of U(VI) as a function of pH.

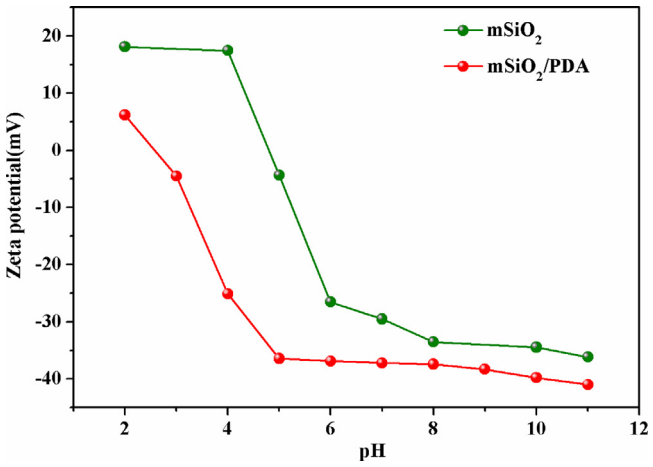

Fig. 14. The zeta potential of $mSiO_2$ and $mSiO_2$/PDA. T = 298.15 K, m/V = 1 g/L.

and $UO_2(OH)_4^{2-}$ become the dominating species when the value of pH persistently increases [61].

To further investigate the influence of pH value on the U(VI) removal, the zeta potentials of $mSiO_2$ and $mSiO_2$/PDA surfaces are characterized. Fig. 14 shows the zeta potential of the $mSiO_2$/PDA surface is lower than the surface of $mSiO_2$. This result is due to the existence of catechol functional groups in PDA layer coated on $mSiO_2$, which also confirms that PDA is successfully coated on the $mSiO_2$ surface. Furthermore, the pH_{pzc} (point of zero charge) of $mSiO_2$/PDA calculated from Fig. 14 is 2.6. This means that the $mSiO_2$/PDA surfaces will be negatively charged when solution pH is above 2.6, which can be benefit for binding the positively charged U(VI) cations with negative $mSiO_2$/PDA surfaces. When pH increases, the binding sites of negatively charged surfaces on $mSiO_2$/PDA arise which enhances the electrostatic interactions with U(VI) cations, making for incre ased U(VI) removal efficiency [70]. The effects of ionic strength on removal U(VI) by $mSiO_2$/PDA are investigated in the presence of $NaNO_3$ solution with concentrations of 0.001, 0.01, 0.1 mol/L, respectively. It is clear that the ionic strength exhibits weak influence on the U(VI) adsorption at all pH values tests, which indicates the adsorption mechanism is inner-sphere surface complexation rather than an ion exchange [8].

3.6. *The cyclability of the $mSiO_2$/PDA in the adsorption of U(VI)*

In order to evaluate the practical application of $mSiO_2$/PDA in the adsorption of U(VI), the regeneration and cycle use experiments were tested. As shown in Fig. 12, the adsorption amount of U(VI) reduced with decreasing pH values, which implied that acid picking is an appropriate method for regeneration. Thus, the 0.01 mol/L HNO_3 is used as desorbing solution to regenerate the adsorbent and adsorption experiments are conducted at 298.15 K, pH = 5.5 ±0.1, $C_{U(VI)}$ (original) = 33 mg/L and m/V = 1 g/L. As presented in Fig. S4, the adsorption capacity of $mSiO_2$/PDA has a decreasing tendency with addition of cycle number. As we know, the desorption of U(VI) from $mSiO_2$/PDA should be conducted in very complicated process in high acid medium. Moreover, $mSiO_2$/PDA nanospheres are mesoporous material with small size and exhibit good water solubility in adsorption experiments. Therefore, the reduced adsorption is mainly attributed to the incomplete desorption of U(VI) from $mSiO_2$/PDA and the loss of adsorbent in cycle process. Most importantly, the adsorption capacity of $mSiO_2$/PDA is also larger than the naked $mSiO_2$ even at more than 4 adsorption-desorption cycles, demonstrating the high performance of $mSiO_2$/PDA. Furthermore, the TEM and SEM were used to determine the changes of structure and the loss of porosity ($mSiO_2$/PDA) after the adsorption-desorption process (Fig. S5). No obvious change is found for the physical structure of $mSiO_2$/PDA after the first cycle, indicating the well stability of the composite structure.

4. Conclusions

In summary, we successfully synthesized the $mSiO_2$/PDA nanospheres with excellent adsorption performance for U(VI) removal via modifying $mSiO_2$ with PDA. The adsorption process could be well described by the pseudo-second-order kinetics model with the equilibrium time within 4 h. The adsorption isotherms of U(VI) on $mSiO_2$/PDA surface were fitted well by the Langmuir model, and the maximum adsorption capacity was 332.3 mg/g at 318.15 K and pH = 5.5. The data of thermodynamic parameters indicated a spontaneous and endothermic adsorption process. In addition, this adsorption process was pH-dependent, while the ionic strength had a slight influence. In conclusion, the as-synthesized $mSiO_2$/PDA could be used as an efficient adsorbent for separation of U(VI) from contaminated water.

Acknowledgements

Financial supports from the National Natural Science Foundation of China (Grant No. 11372301, 11572310), the fundamental research funds for the Central Universities (WK2480000002), and the Strategic Priority Research Program of the Chinese Academy of Sciences (Grant No. XDB22040502) are gratefully acknowledged. This study was also supported by the Collaborative Innovation Center of Suzhou Nano Science and Technology.

Appendix A. Supplementary data

Supplementary data associated with this article can be found, in the online version, at http://dx.doi.org/10.1016/j.apsusc.2017.07.274.

References

[1] H. Nifenecker, Future electricity production methods. Part 1: nuclear energy, Rep. Prog. Phys. 74 (2011) 1–28.
[2] M. Asif, T. Muneer, Energy supply, its demand and security issues for developed and emerging economies, Renew. Sustain. Energy Rev. 11 (2007) 1388–1413.
[3] A. Hosseini, J.E. Brown, J.P. Gwynn, M. Dowdall, Review of research on impacts to biota of discharges of naturally occurring radionuclides in produced water to the marine environment, Sci. Total Environ. 438 (2012) 325–333.
[4] P.C. Burns, R.C. Ewing, A. Navrotsky, Nuclear fuel in a reactor accident, Science 335 (2012) 1184–1188.

[5] M. Anke, O. Seeber, R. Müller, U. Schäfer, J. Zerull, Uranium transfer in the food chain from soil to plants, animals and man, Chem. Erde-Geochem. 69 (2009) 75–90.
[6] L. Zhou, M. Bosscher, C. Zhang, S. Ozcubukcu, L. Zhang, W. Zhang, C.J. Li, J. Liu, M.P. Jensen, L. Lai, C. He, A protein engineered to bind uranyl selectively and with femtomolar affinity, Nat. Chem. 6 (2014) 236–241.
[7] S. Duan, X. Liu, Y. Wang, D. Shao, N.S. Alharbi, A. Alsaedi, J. Li, Highly efficient entrapment of U (VI) by using porous magnetic $Ni_{0.6}Fe_{2.4}O_4$ micro-particles as the adsorbent, J. Taiwan.Inst. Chem. Eng. 65 (2016) 367–377.
[8] X. Liu, J. Li, X. Wang, C. Chen, X. Wang, High performance of phosphate-functionalized graphene oxide for the selective adsorption of U (VI) from acidic solution, J. Nucl. Mater. 466 (2015) 56–64.
[9] R. Zhang, C. Chen, J. Li, X. Wang, Investigation of interaction between U (VI) and carbonaceous nanofibers by batch experiments and modeling study, J. Colloid Interface Sci. 460 (2015) 237–246.
[10] A. Favre-Réguillon, G. Lebuzit, D. Murat, J. Foos, C. Mansour, M. Draye, Selective removal of dissolved uranium in drinking water by nanofiltration, Water Res. 42 (2008) 1160–1166.
[11] A.C.Q. Ladeira, C.R. Gonçalves, Influence of anionic species on uranium separation from acid mine water using strong base resins, J. Hazard. Mater. 148 (2007) 499–504.
[12] A. Krivoruchko, I. Atamanenko, L.Y. Yurlova, Removal of uranium from waters with the various salt content by the ultrafiltration method, J. Water Chem. Technol. 33 (2011) 97–106.
[13] C. Ding, W. Cheng, Y. Sun, X. Wang, Novel fungus-Fe_3O_4 bio-nanocomposites as high performance adsorbents for the removal of radionuclides, J. Hazard. Mater. 295 (2015) 127–137.
[14] W. Li, Q. Liu, J. Liu, H. Zhang, R. Li, Z. Li, X. Jing, J. Wang, U. Removal, (VI) from artificial seawater using facilely and covalently grafted polyacrylonitrile fibers with lysine, Appl. Surf. Sci. 403 (2017) 378–388.
[15] D.L. Guerra, V.L. Leidens, R.R. Viana, C. Airoldi, Amazon kaolinite functionalized with diethylenetriamine moieties for U (VI) removal: thermodynamic of cation-basic interactions, J. Hazard. Mater. 180 (2010) 683–692.
[16] M. Xu, G. Wei, N. Liu, L. Zhou, C. Fu, M. Chubik, A. Gromov, W. Han, Novel fungus?titanate bio-nanocomposites as high performance adsorbents for the efficient removal of radioactive ions from wastewater, Nanoscale 6 (2014) 722–725.
[17] Y. Xie, E.M. Helvenston, L.C. Shuller-Nickles, B.A. Powell, Surface complexation modeling of Eu (III) and U (VI) interactions with graphene oxide, Environ. Sci. Technol. 50 (2016) 1821–1827.
[18] S. Yakout, S. Metwally, T. El-Zakla, Uranium sorption onto activated carbon prepared from rice straw: competition with humic acids, Appl. Surf. Sci. 280 (2013) 745–750.
[19] Y. Wang, Z. Gu, J. Yang, J. Liao, Y. Yang, N. Liu, J. Tang, Amidoxime-grafted multiwalled carbon nanotubes by plasma techniques for efficient removal of uranium (VI), Appl. Surf. Sci. 320 (2014) 10–20.
[20] L. Chen, D. Zhao, S. Chen, X. Wang, C. Chen, One-step fabrication of amino functionalized magnetic graphene oxide composite for uranium (VI) removal, J.Colloid Interface Sci. 472 (2016) 99–107.
[21] T. Anirudhan, C. Bringle, S. Rijith, Removal of uranium (VI) from aqueous solutions and nuclear industry effluents using humic acid-immobilized zirconium-pillared clay, J. Environ. Radioact. 101 (2010) 267–276.
[22] X. Wang, D. Shao, G. Hou, X. Wang, A. Alsaedi, B. Ahmad, Uptake of Pb (II) and U (VI) ions from aqueous solutions by the ZSM-5 zeolite, J. Mol. Liq. 207 (2015) 338–342.
[23] S. Aytas, S. Akyil, M. Eral, Adsorption and thermodynamic behavior of uranium on natural zeolite, J. Radioanal. Nucl. Chem. 260 (2004) 119–125.
[24] X. Guo, Y. Feng, L. Ma, D. Gao, J. Jing, J. Yu, H. Sun, H. Gong, Y. Zhang, Phosphoryl Functionalized Mesoporous Silica for Uranium Adsorption, Appl. Surf. Sci. 402 (2017) 53–60.
[25] D. Li, S. Egodawatte, D.I. Kaplan, S.C. Larsen, S.M. Serkiz, J.C. Seaman, Functionalized magnetic mesoporous silica nanoparticles for U removal from low and high pH groundwater, J. Hazard. Mater. 317 (2016) 494–502.
[26] Y. Liu, Q. Li, X. Cao, Y. Wang, X. Jiang, M. Li, M. Hua, Z. Zhang, Removal of uranium (VI) from aqueous solutions by CMK-3 and its polymer composite, Appl. Surf. Sci. 285 (2013) 258–266.
[27] W. Um, S. Mattigod, R.J. Serne, G.E. Fryxell, D.H. Kim, L.D. Troyer, Synthesis of nanoporous zirconium oxophosphate and application for removal of U (VI), Water Res. 41 (2007) 3217–3226.
[28] J.L. Vivero-Escoto, M. Carboni, C.W. Abney, W. Lin, Organo-functionalized mesoporous silicas for efficient uranium extraction, Microporous Mesoporous Mater. 180 (2013) 22–31.
[29] K. Vidya, S. Dapurkar, P. Selvam, S. Badamali, N. Gupta, The entrapment of UO_2^{2+} in mesoporous MCM-41 and MCM-48 molecular sieves, Microporous Mesoporous Mater. 50 (2001) 173–179.
[30] Y. Zhao, X. Wang, J. Li, X. Wang, Amidoxime functionalization of mesoporous silica and its high removal of U (VI), Polym. Chem. 6 (2015) 5376–5384.
[31] H.I. Lee, J.H. Kim, J.M. Kim, S. Kim, J.-N. Park, J.S. Hwang, J.-W. Yeon, Y. Jung, Application of ordered nanoporous silica for removal of uranium ions from aqueous solutions, J. Nanosci. Nanotechnol. 10 (2010) 217–221.
[32] L.-Y. Yuan, Y.-L. Liu, W.-Q. Shi, Y.-L. Lv, J.-H. Lan, Y.-L. Zhao, Z.-F. Chai, High performance of phosphonate-functionalized mesoporous silica for U (VI) sorption from aqueous solution, Dalton Trans. 40 (2011) 7446–7453.
[33] H. Lee, S.M. Dellatore, W.M. Miller, P.B. Messersmith, Mussel-inspired surface chemistry for multifunctional coatings, Science 318 (2007) 426–430.
[34] Y. Mao, W. Jiang, S. Xuan, Q. Fang, K.C.-F. Leung, B.S. Ong, S. Wang, X. Gong, Rod-like β-FeOOH@poly(dopamine)–Au–poly(dopamine) nanocatalysts with improved recyclable activities, Dalton Trans. 44 (2015) 9538–9544.
[35] M. Liu, W. Jiang, Q. Chen, S. Wang, Y. Mao, X. Gong, K.C.-F. Leung, J. Tian, H. Wang, S. Xuan, A facile one-step method to synthesize SiO_2@polydopamine core–shell nanospheres for shear thickening fluid, RSC Adv. 6 (2016) 29279–29287.
[36] M. Zhou, Q. Liu, S. Wu, Z. Gou, X. Wu, D. Xu, Starch/chitosan films reinforced with polydopamine modified MMT: effects of dopamine concentration, Food Hydrocolloids 61 (2016) 678–684.
[37] Y. Dong, T. Liu, S. Sun, X. Chang, N. Guo, Preparation and characterization of SiO 2/polydopamine/Ag nanocomposites with long-term antibacterial activity, Ceram. Int. 40 (2014) 5605–5609.
[38] X. Li, H. Lu, Y. Zhang, F. He, L. Jing, X. He, Fabrication of magnetic alginate beads with uniform dispersion of $CoFe_2O_4$ by the polydopamine surface functionalization for organic pollutants removal, Appl. Surf. Sci. 389 (2016) 567–577.
[39] Q. Ye, F. Zhou, W. Liu, Bioinspired catecholic chemistry for surface modification, Chem. Soc. Rev. 40 (2011) 4244–4258.
[40] Z. Zhao, J. Li, T. Wen, C. Shen, X. Wang, A. Xu, Surface functionalization graphene oxide by polydopamine for high affinity of radionuclides, Colloids Surf. A 482 (2015) 258–266.
[41] C. Cheng, S. Li, J. Zhao, X. Li, Z. Liu, L. Ma, X. Zhang, S. Sun, C. Zhao, Biomimetic assembly of polydopamine-layer on graphene: mechanisms, versatile 2D and 3D architectures and pollutant disposal, Chem. Eng. J. 228 (2013) 468–481.
[42] J. Jiang, L. Zhu, L. Zhu, B. Zhu, Y. Xu, Surface characteristics of a self-polymerized dopamine coating deposited on hydrophobic polymer films, Langmuir 27 (2011) 14180–14187.
[43] X. Zheng, J. Zhang, J. Wang, X. Qi, J.M. Rosenholm, K. Cai, Polydopamine coatings in confined nanopore space: toward improved retention and release of hydrophilic cargo, J. Phys. Chem. C 119 (2015) 24512–24521.
[44] X. Zheng, F. Chen, J. Zhang, K. Cai, Silica-assisted incorporation of polydopamine into the framework of porous nanocarriers by a facile one-pot synthesis, J. Mater. Chem. B 4 (2016) 2435–2443.
[45] Q. Zheng, T. Lin, H. Wu, L. Guo, P. Ye, Y. Hao, Q. Guo, J. Jiang, F. Fu, G. Chen, Mussel-inspired polydopamine coated mesoporous silica nanoparticles as pH-sensitive nanocarriers for controlled release, Int. J. Pharm. 463 (2014) 22–26.
[46] T. Ataei-Germi, A. Nematollahzadeh, Bimodal porous silica microspheres decorated with polydopamine nano-particles for the adsorption of methylene blue in fixed-bed columns, J. Colloid Interface Sci. 470 (2016) 172–182.
[47] Y. Chen, J. Gao, X. Wen, W. Wu, Efficient removal of cadmium using facile functionalized of mesoporous silica via a biomimetic coating, RSC Adv. 6 (2016) 18340–18347.
[48] Z.-A. Qiao, L. Zhang, M. Guo, Y. Liu, Q. Huo, Synthesis of mesoporous silica nanoparticles via controlled hydrolysis and condensation of silicon alkoxide, Chem. Mater. 21 (2009) 3823–3829.
[49] Y. Chen, J. Gao, X. Wen, W. Wu, Efficient removal of cadmium using facile functionalized of mesoporous silica viaa biomimetic coating, RSC Adv. 6 (2016) 18340–18347.
[50] N. Fellenz, F.J. Perez-Alonso, P.P. Martin, J.L. García-Fierro, J.F. Bengoa, S.G. Marchetti, S. Rojas, Chromium (VI) removal from water by means of adsorption-reduction at the surface of amino-functionalized MCM-41 sorbents, Microporous Mesoporous Mater. 239 (2017) 138–146.
[51] S. Abbasizadeh, A.R. Keshtkar, M.A. Mousavian, Preparation of a novel electrospun polyvinyl alcohol/titanium oxide nanofiber adsorbent modified with mercapto groups for uranium (VI) and thorium (IV) removal from aqueous solution, Chem. Eng. J. 220 (2013) 161–171.
[52] X. Zhang, C. Jiao, J. Wang, Q. Liu, R. Li, P. Yang, M. Zhang, Removal of uranium (VI) from aqueous solutions by magnetic Schiff base: kinetic and thermodynamic investigation, Chem. Eng. J. 198 (2012) 412–419.
[53] M. Song, Q. Wang, Y. Meng, Removal of UO_2^{2+} from aqueous solution by plasma functionalized MWCNTs, J. Radioanal. Nucl. Chem. 293 (2012) 899–906.
[54] E. Bulut, M. Özacar, İ.A. Şengil, Adsorption of malachite green onto bentonite: equilibrium and kinetic studies and process design, Microporous Mesoporous Mater. 115 (2008) 234–246.
[55] R. Zhang, C. Chen, J. Li, X. Wang, Preparation of montmorillonite@carbon composite and its application for U (VI) removal from aqueous solution, Appl. Surf. Sci. 349 (2015) 129–137.
[56] A. Rahmani-Sani, A. Hosseini-Bandegharaei, S.-H. Hosseini, K. Kharghani, H. Zarei, A. Rastegar, Kinetic, equilibrium and thermodynamic studies on sorption of uranium and thorium from aqueous solutions by a selective impregnated resin containing carminic acid, J. Hazard. Mater. 286 (2015) 152–163.
[57] W.W. Ngah, M. Hanafiah, S. Yong, Adsorption of humic acid from aqueous solutions on crosslinked chitosan–epichlorohydrin beads: kinetics and isotherm studies, Colloids Surf. B 65 (2008) 18–24.
[58] M.A. Alavijeh, M.N. Sarvi, Z.R. Afarani, Properties of adsorption of vitamin B12 on nanoclay as a versatile carrier, Food Chem. 219 (2017) 207–214.
[59] N.Y. Mezenner, A. Bensmaili, Kinetics and thermodynamic study of phosphate adsorption on iron hydroxide-eggshell waste, Chem. Eng. J. 147 (2009) 87–96.
[60] G. Boyd, A. Adamson, L. Myers Jr., The exchange adsorption of ions from aqueous solutions by organic zeolites. II. Kinetics1, J. Am. Chem. Soc. 69 (1947) 2836–2848.

[61] W. Song, M. Liu, R. Hu, X. Tan, J. Li, Water-soluble polyacrylamide coated-Fe_3O_4 magnetic composites for high-efficient enrichment of U (VI) from radioactive wastewater, Chem. Eng. J. 246 (2014) 268–276.
[62] L.-Y. Yuan, Y.-L. Liu, W.-Q. Shi, Z. -j. Li, J.-H. Lan, Y.-X. Feng, Y.-L. Zhao, Y.-L. Yuan, Z.-F. Chai, A novel mesoporous material for uranium extraction, dihydroimidazole functionalized SBA-15, J. Mater. Chem. 22 (2012) 17019–17026.
[63] J. Li, Z. Guo, S. Zhang, X. Wang, Enrich and seal radionuclides in magnetic agarose microspheres, Chem. Eng. J. 172 (2011) 892–897.
[64] Y. Zhao, J. Li, S. Zhang, X. Wang, Amidoxime-functionalized magnetic mesoporous silica for selective sorption of U (VI), RSC Adv. 4 (2014) 32710–32717.
[65] J. Li, X. Yang, C. Bai, Y. Tian, B. Li, S. Zhang, X. Yang, S. Ding, C. Xia, X. Tan, A novel benzimidazole-functionalized 2-D COF material: synthesis and application as a selective solid-phase extractant for separation of uranium, J. Colloid Interface Sci. 437 (2015) 211–218.
[66] I.I. Fasfous, J.N. Dawoud, Uranium (VI) sorption by multiwalled carbon nanotubes from aqueous solution, Appl. Surf. Sci. 259 (2012) 433–440.
[67] C. Gok, S. Aytas, Biosorption of uranium (VI) from aqueous solution using calcium alginate beads, J. Hazard. Mater. 168 (2009) 369–375.
[68] P. Zong, S. Wang, Y. Zhao, H. Wang, H. Pan, C. He, Synthesis and application of magnetic graphene/iron oxides composite for the removal of U (VI) from aqueous solutions, Chem. Eng. J. 220 (2013) 45–52.
[69] Y.-Q. Wang, Z.-B. Zhang, Y.-H. Liu, X.-H. Cao, Y.-T. Liu, Q. Li, Adsorption of U (VI) from aqueous solution by the carboxyl-mesoporous carbon, Chem. Eng. J. 198 (2012) 246–253.
[70] D. Shao, J. Li, X. Tan, Z. Yang, K. Okuno, Y. Oya, XPS investigation of impurities containing boron films affected by energetic deuterium implantation and thermal desorption, J. Nucl. Mater. 457 (2015) 118–123.